Journal of Alloys and Compounds 495 (2010) 611–616

Contents lists available at ScienceDirect

Journal of Alloys and Compounds

journal homepage: www.elsevier.com/locate/jallcom

Nanostructured alumina coatings manufactured by air plasma spraying: Correlation of properties with the raw powder microstructure

D. Zois[a,b], A. Lekatou[b,*], M. Vardavoulias[a], A. Vazdirvanidis[c]

[a] Pyrogenesis SA, Technological Park of Lavrion, 19500 Lavrion, Greece
[b] University of Ioannina, Department of Materials Science & Engineering, 45110 Ioannina, Greece
[c] Hellenic Centre for Metal Research, Pireos 252, 17778 Athens, Greece

ARTICLE INFO

Article history:
Received 3 July 2008
Received in revised form 9 October 2009
Accepted 12 October 2009
Available online 20 October 2009

Keywords:
Nanostructured alumina
Coating materials
Sintering
X-ray diffraction
SEM

ABSTRACT

High energy ball milled nanostructured Al_2O_3 ("N"), fused/crushed conventional Al_2O_3 ("C") and sintered nanostructured Al_2O_3 ("S") powders were air plasma sprayed on 304 stainless steel. The nanostructured powder was composed of nanoparticle agglomerates, whereas the conventional powder consisted of solid granules. The average crystal size of the powders was estimated by X-ray diffraction based methods (the Scherrer equation and the Williamson Hall plot). Deviations between the crystal sizes calculated by the two methods indicated high lattice strain induced by the nanopowder production technique. Sintering of the nanopowder did not cause any considerable grain growth; moreover, the strain was alleviated. The melting degree of the powders, reflected by the γ-Al_2O_3 content of the coatings, depended on their porosities. Coatings "N" presented the lowest melting degree due to the inherent porosity of the agglomerated nanoparticles composing powder "N". As a result, their microstructure was characterized by high porosity and extensive microcracking. The "S" coatings exhibited higher melting degree than that of the "N" coatings (similar to that of the "C" coatings), due to a tighter microstructure attained by sintering. At the same time, part of the initial nanostructure had been preserved during sintering and spraying. The "S" coatings presented the highest adhesion because they combined a high melting degree with pockets of retained nanostructure; the latter could act as crack arresters. Increasing the spray power led to an increase in the melting degree and, consequently, a decrease in the coating porosity and an increase in the porosity affected properties (adhesion and hardness).

1. Introduction

Nanostructured bulk materials exhibit considerably higher tensile strength, fracture toughness, hardness and wear resistance when compared to their microstructured counterparts. These improvements are associated with grain sizes smaller than 100 nm [1–4]. Various thermal spraying techniques have been employed to prepare nanostructured oxide-based coatings, such as: high velocity oxygen fuel-HVOF (TiO_2) [5,6], vacuum plasma spray-VPS (TiO_2) [7], plasma spraying of liquid precursors (ZrO_2, $Al2O_3$, TiO_2) [8], atmospheric plasma spraying-APS (TiO_2) [5], Al_2O_3–TiO_2 [9–11], ZrO_2 [12]. TiO_2 and Al_2O_3–TiO_2 nanostructured coatings have been reported to possess superior wear resistance, adhesion, toughness and spallation resistance than their conventional counterparts [6,10,11].

Amongst nanoparticle production techniques, such as sol–gel synthesis, inert gas condensation and high energy milling [13–15], the latter is commonly used to produce large quantities of nanopowders, because it is a low cost process and is applicable to a variety of materials [15]. High energy ball milling is, by far, more effective than conventional ball milling in reducing particle size; however, it induces high strains to the milled particles.

Lin et al. [16] reported that sintering of alumina–3 wt% titania nanopowder can increase the density of the granules and assist spherical shape retention during plasma spraying. By sintering, fragmentation of the granules is avoided; very fine particles would not possess the momentum to infiltrate the flame stream or, in the case of entering the flame, they would rapidly get melted [17], eliminating any nanostructure. No considerable growth has been noticed after sintering of nano- and sub-micron alumina in the temperature range 1150–1275 °C [18,19]. Chinelatto et al. [20] sintered high energy milled nanostructured α-Al_2O_3 powder in two stages: At the first stage (950 °C), surface diffusion occurred; it did not cause any significant densification, but led to smoothing of the agglomerate surface and coalescence of the finest and coarsest particles. At the second stage (1300 °C), the density and grain size were significantly increased. The sintering temperature for α-Al_2O_3 agglomerate-free nanopowder should be about 300–400 °C

* Corresponding author. Tel.: +30 26510 97309; fax: +30 26510 97034.
E-mail address: alekatou@cc.uoi.gr (A. Lekatou).

0925-8388/$ – see front matter © 2009 Elsevier B.V. All rights reserved.
doi:10.1016/j.jallcom.2009.10.055

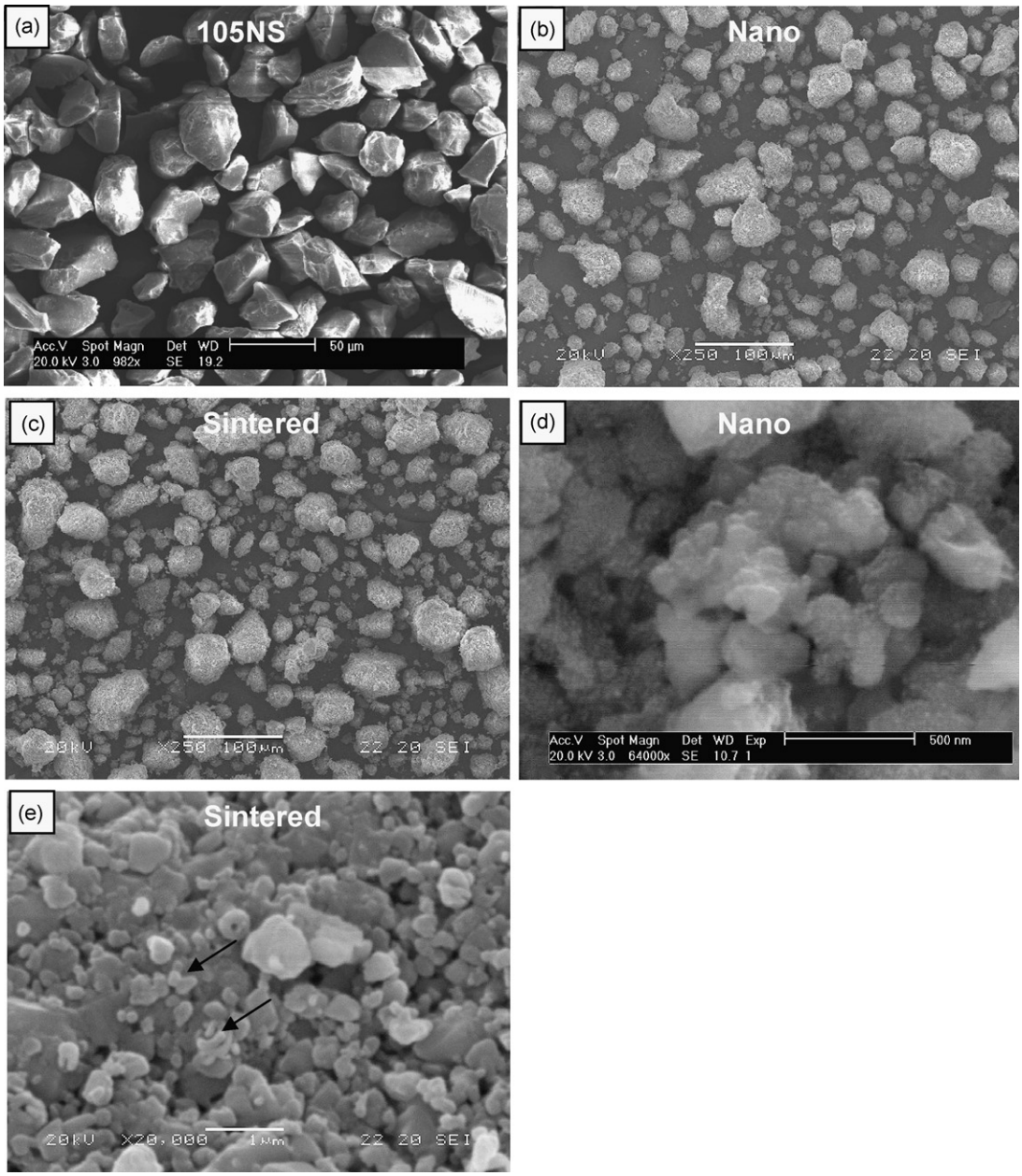

Fig. 1. The feedstock: (a) Conventional crushed and fused powder. (b) High energy ball milled nanopowder. (c) The nanopowder after sintering (1100 °C, 2 h). Agglomerates of nanoparticles, (d) as received, (e) after sintering.

lower than that for Al_2O_3 micropowder [21,22], because of a lower activation energy in comparison to the alumina micropowder.

In the present work, the effect of three different types of raw powders (high energy ball milled nanostructured Al_2O_3, sintered nanostructured Al_2O_3 and conventional fused/crushed conventional Al_2O_3) on characteristic properties of air plasma sprayed coatings, is studied. This work has been conducted within the framework of investigating the potential replacement of conventional alumina coatings in thread and fibre high temperature applications with advanced coatings for improved wear and erosion performance.

2. Experimental

The nanopowder, of particle size (−53 + 10) μm, was produced by a laboratory high energy ball mill. The conventional powder, of nominal particle size (−45 + 15) μm, was Sulzer Metco's 105NS. Spraying was performed by a MiniGun torch (Pyrogenesis Inc) upon 304 stainless steel coupons. Coating porosities and microstructures were evaluated by optical microscopy (Leica DMLM) and SEM-EDX

Table 1
Crystal sizes and strains of the feedstocks.

Material	Crystal size—Scherrer (nm)	Crystal size—Williamson Hall (nm)	Strain—Williamson Hall (%)
Conventional powder ("C")	≫100	≫100	0.00
Nano powder ("N")	24	93	1.15
Sintered nano powder ("S")	122	>100	0.20

(Philips XL 40 SFEG and JEOL JSM 5600). Microhardness (14 measurements per coating) was measured by a Shimadzu tester. Adhesion was determined on the principle of applying a controlled pneumatic force to a piston stud glued to the coating. Three measurements per coating were conducted by a portable elcometer (110 P.A.T.T.I.), according to the ASTM C633-01 standard. Sintering was carried out in a Nabertherm box furnace (air, 1100 °C, 2 h). X-ray diffraction patterns were obtained by a Bruker D8 Advance diffractometer. The nanocrystalline size was calculated by two XRD-based methods, the Scherrer equation and the Williamson Hall plot. The former is only capable of defining crystal sizes, while the latter is also capable of calculating lattice strain [23]. Phase percentages in powders and coatings were determined by the XRD-based Rietveld analysis [24].

3. Results and discussion

3.1. Feedstock characterization

Fig. 1a–c illustrates the morphologies of the conventional ("C"), nanostructured ("N") and sintered ("S") powders, respectively. Powder "C" consists of solid irregular granules, whereas powders "N" and "S" consist of agglomerates of nanoparticles having smooth shapes (a typical morphological result of the milling process [15]). Agglomerates of nanoparticles "N" are discerned in Fig. 1d. Macroscopically, both sintered and "green" nanopowders present similar morphologies and particle sizes. Therefore, it is considered that the main sintering mechanism is material redistribution, aiming at decreasing the surface energy of particles by reducing their available surface area. Indeed, on closer examination (and in compatibility with previous works [20]), smoothing of the agglomerate surface and a decrease in the finer particles can be discerned. The latter have either been consolidated or embodied to the coarser ones (Fig. 1e); as finer particles have a higher area-to-volume ratio, the spontaneity to reduce their surface energy is higher, causing their consolidation. Coalescence occurs by necking (pointed by arrows in Fig. 1e), which is typical for alumina [25].

The XRD patterns of Fig. 2 reveal that the main phase in the three powders is α-Al_2O_3. Al and α-Fe are also detected in powder "N" (1.1 and 1.14 wt%, respectively, as determined by Rietveld analysis). The stoichiometry used in the powder production is the main reason for the aluminium presence. The iron presence suggests powder contamination by the tool steel balls and vials of the ball mill. Powder "N" presents the widest peaks amongst the feedstocks, suggesting nanocrystalline dimensions and possible non-uniform strain exertion. Powder "S" presents narrower peaks, though wider than the "C" powder peaks, indicating considerable presence of submicron crystals. Sintering has caused oxidation of Fe to Fe_2O_3, in free form and in solution with Al_2O_3.The latter is indicated by the α-phase peak displacement at lower angles (Fig. 2).

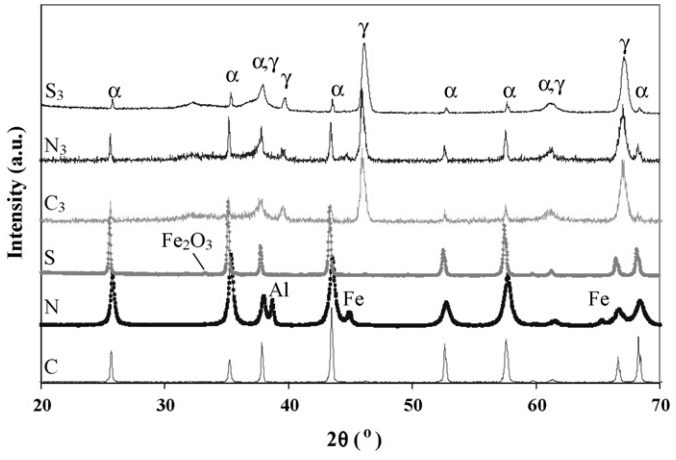

Fig. 2. XRD patterns of the three powders and their coatings. α: α-Al_2O_3, γ: γ-Al_2O_3.

Table 1 lists the nanopowder crystal sizes calculated by the Scherrer equation and Williamson Hall plot. These methods are considered quite accurate for particle sizes less than 100 nm; beyond this limit, accuracy gradually decreases with size [26,27]. Therefore, they do not provide any information about the crystal size of powder "C". The quite different crystal sizes of powder "N", estimated by the two methods, are owing to lattice strain. The consecutive high energy impacts during milling induced high strain and distortion in the grains, which were imprinted on the peak widths. The Williamson Hall method, being capable of distinguishing between size and strain contribution, yields more accurate crystal size values. Table 1 also shows that sintering has caused strain relief, serving as an annealing stage. The grain sizes calculated by Scherrer and Williamson Hall would possibly be similar for the "S" powder, if accurate Williamson Hall calculations in the sub-micron range were feasible.

3.2. Characterization of the deposited coatings

A major issue in spraying nanoparticles is the retention of part of the original nanostructure in the coating, in order to maintain

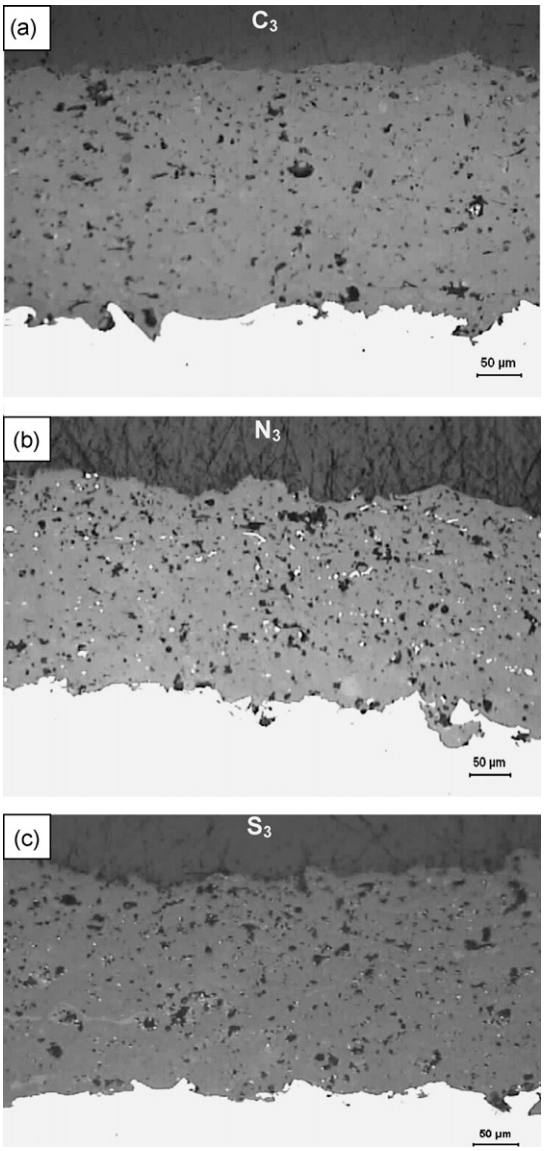

Fig. 3. Overview cross-sections of the coatings: (a) "C_3", (b) "N_3", (c) "S_3".

Table 2
Quantitative phase analysis and properties of the coatings.

Designation	Spraying power (kW)	α-Al_2O_3 (wt%)	γ-Al_2O_3 (wt%)	Porosity (%)	Adhesion (MPa)	Hardness (HV_{100})
C_1	25	18.1–23.2	76.8–81.9	6.6 ± 0.6	17.6 ± 0.9	1063 ± 145
C_2	32	9.1–10.8	89.2–90.9	6.1 ± 0.7	18.1 ± 1.5	1078 ± 259
C_3	39	8.3–9.9	90.1–91.7	5.5 ± 0.8	19.8 ± 1.6	1127 ± 105
N_1	25	51.9–54.6	45.4–48.1	15.3 ± 5.8	10.5 ± 0.8	972 ± 120
N_2	32	48.0–52.0	52.0–48.0	13.2 ± 2.0	11.4 ± 1.3	1070 ± 166
N_3	39	17.1–23.3	76.7–82.9	10.0 ± 0.1	17.7 ± 2.4	1131 ± 128
S_1	25	14.9–19.7	80.3–85.1	7.3 ± 1.5	24.1 ± 2.1	1034 ± 152
S_2	32	12.8–15.3	84.7–87.2	7.7 ± 2.6	23.4 ± 1.8	1065 ± 179
S_3	39	10.3–11.5	88.5–89.7	5.9 ± 0.5	26.3 ± 2.2	1109 ± 122

its beneficial effect on the properties. On the other hand, coatings must exhibit integrity, cohesion and adhesion, which can only be achieved by a sufficient degree of particle melting; the latter eliminates nanostructure.

Cross-sections of the manufactured coatings are illustrated in Fig. 3. The coatings seem uniform and fairly adherent to the substrate. Table 2 quantifies the microstructure related properties and the phase composition of the coatings.

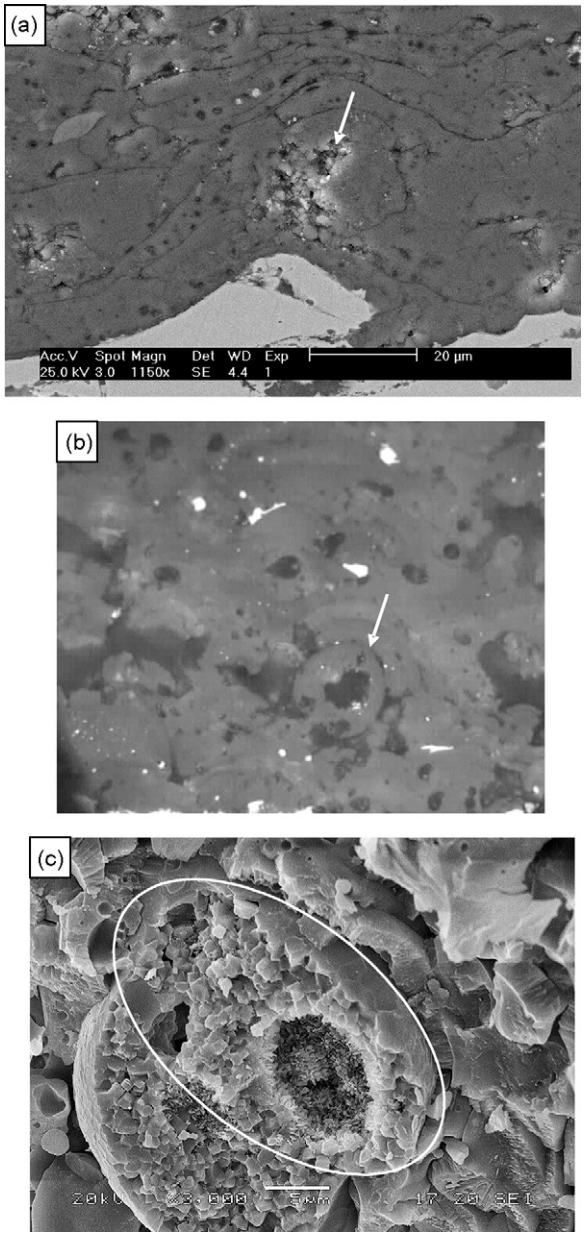

Fig. 4. Cross-sections of coating "N" showing: (a) a pocket of semi-molten nanoparticles associated with an asperity in "N_1", (b) hollow spherical particles in "N_1", (c) a fractured surface of semi-molten particles in "N_3"; low in-particle cohesion generates their splitting.

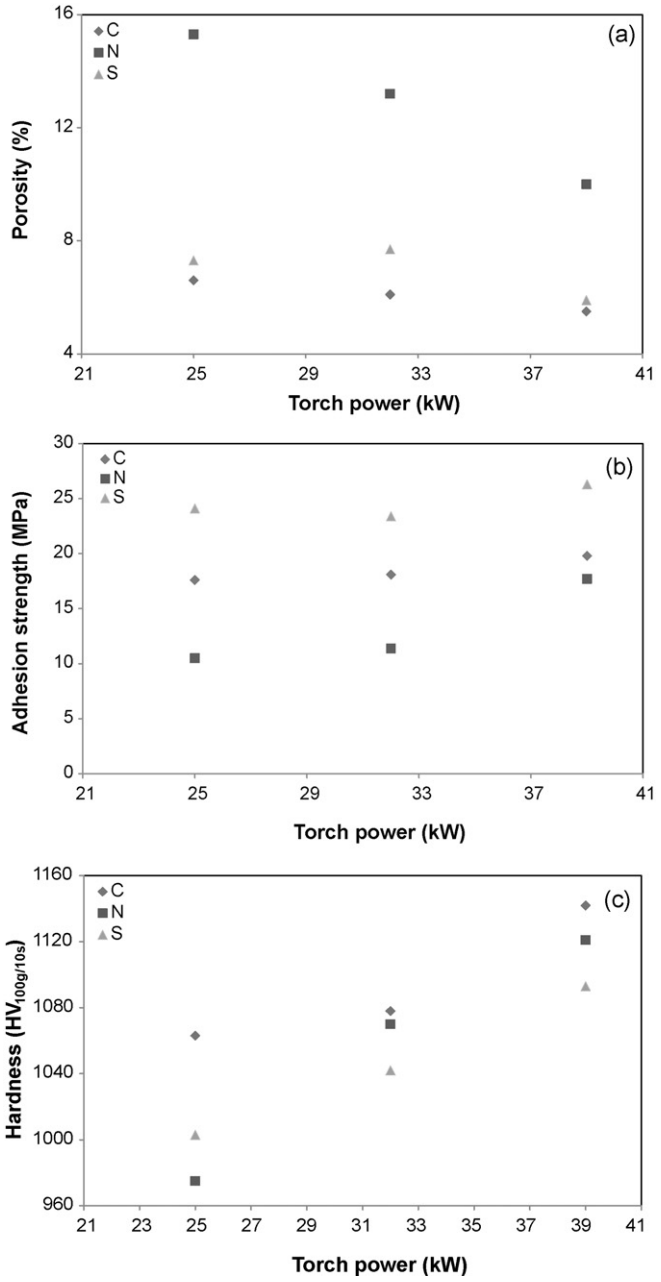

Fig. 5. Coating properties vs. torch power: (a) porosity, (b) adhesion, (c) hardness.

3.2.1. Correlation of the powder microstructure to the coating microstructure

The coatings consist of α-Al_2O_3 and γ-Al_2O_3, as shown in the XRD patterns of Fig. 2. γ-Al_2O_3 results from rapid quenching of molten Al_2O_3. α-Al_2O_3 corresponds to the unmelted α-Al_2O_3 fraction in the powder [28]. γ-Al_2O_3 has a lower energy barrier for nucleation than α-Al_2O_3 [29] leading to its preferential nucleation.

Table 2 shows that at low and medium spraying power, the α-Al_2O_3 content of the "N" coatings is notably higher than that of the "C" and "S" counterparts. This suggests that, during spraying, a large fraction of the initial nanoparticles "N" remained unmelted. The lower melting degree of feedstock "N" is attributed to the inherent porosity of the "green" agglomerated nanoparticles: Being compact bodies, conventional particles ("C") or even sintered nanoparticles ("S") exhibit higher thermal conductivity than their porous counterparts ("N") [30]. From a microstructure standpoint, the low melting degree of the "N" coatings is reflected by: (a) a high percentage of partially deformed semi-molten particles, which are incapable of filling any asperities and gaps of the previously deposited layers (Fig. 4 a); and (b) a high presence of semi-molten spheroid particles with large internal voids (Fig. 4b and c). Their formation is attributed to air impelling through internal capillaries towards the core of the agglomerated particles ("N") and subsequent heat induced expansion [31]. This phenomenon was also encountered in the "S" coatings but at a lower extent, as the tighter structure prevented the impelling of large air quantities.

Table 2 shows that the "S" particles have attained slightly lower melting degrees than their "C" counterparts. The tighter structure of the "S" particles due to sintering consequences, such as (limited) nanoparticle coalescence and increased intraparticle cohesion, has increased their thermal conductivity, leading to melting degrees that are comparable to those of the "C" particles.

3.2.2. Correlation of the coating microstructure to the coating properties

Fig. 5 presents the trends of porosity, adhesion strength and hardness vs. torch power for the three types of coatings.

As a consequence of their lower melting degree, the "N" coatings present higher porosities than the "C" and "S" counterparts (Figs. 3 and 5). Fig. 5b demonstrates that the adhesion strength of the coatings increases with decreasing porosity; thus, the "N" coatings present the lowest adhesion. Fig. 4c illustrates the fractured surface of semi-molten deposited particles "N": Cohesion and not adhesion (to the substrate) failure was the actual reason for the coating failure. Two factors contributed to this: (i) The increased porosity of the "N" coatings and (ii) the loose structure of the unmolten "N" agglomerates that was unable to maintain its integrity under tensile forces.

Coatings "S" present significantly higher adhesion in comparison not only to the nanostructured but also to the conventional counterparts, regardless of the spraying power. This increase in adhesion is attributed to: (a) sintering consequences, such as increased intraparticle cohesion, particle coalescence to submicron particles (Fig. 1e), as well as strain relief (Table 1); the positive effect of sintering on the intraparticle cohesion and the

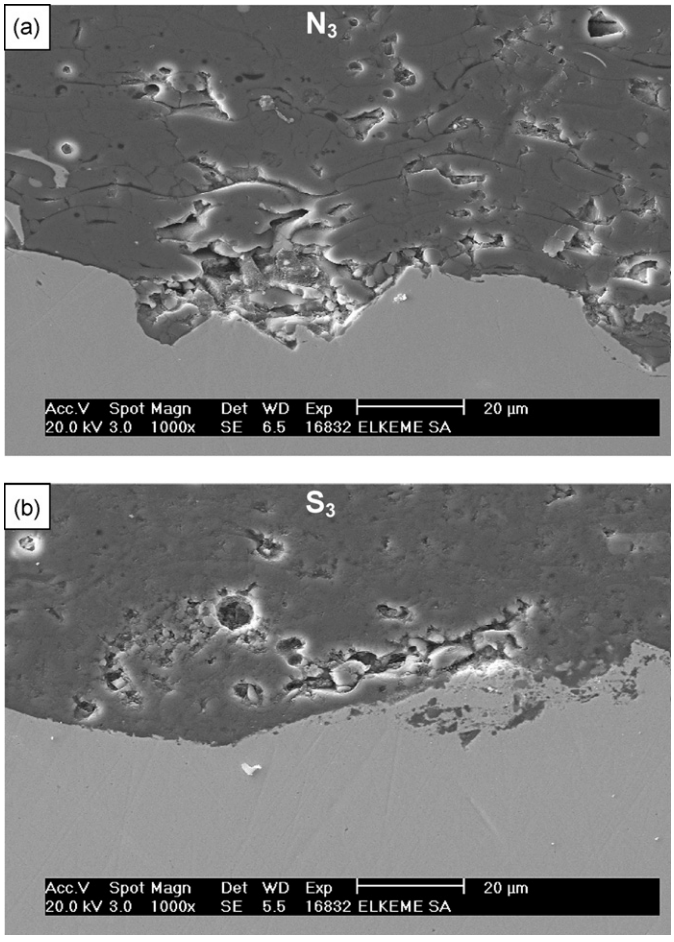

Fig. 6. Coating-substrate interfaces: (a) "N_3", (b) "S_3". The "N_3" coating presents a looser interface with notably more intensive microcracking in its vicinity.

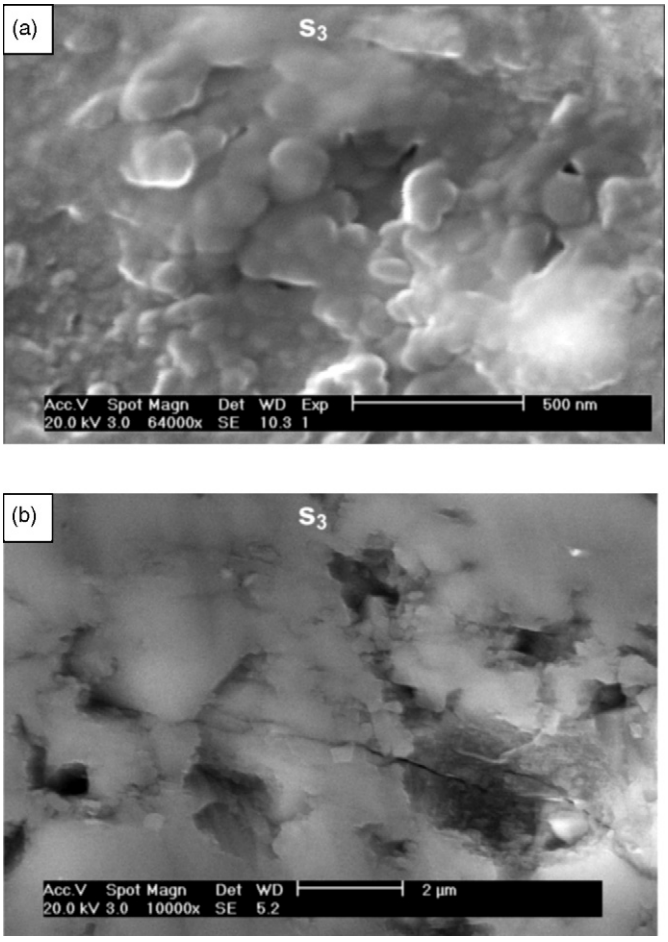

Fig. 7. (a) A semi-molten pocket in coating "S_3" showing that the initial nanostructure has been retained. (b) The nanozone can hinder crack propagation in coating "S_3".

consequent enhancement of the mechanical anchoring between consecutive splats is suggested by the reduction of microcracking in the respective coating structure (Fig. 6) and (b) nanostructure retaining; despite the similar fractions of molten phase in coatings "S" and "C" (Table 2), coatings "S" have retained part of the powder nanostructure, as illustrated in Fig. 7a. The retained nanostructure can hinder crack propagation, as demonstrated in Fig. 7b.

Table 2 shows that coatings "N" exhibit similar hardnesses with coatings "C" and "S". This can be explained by the employment of a small indentation load, so that the hardness values depended to a major extent on the intrinsic properties of the materials and to a less extent on their extrinsic characteristics (e.g. pores, defects).

3.2.3. Correlation of the spray power to the coating microstructure and properties

The properties of the coatings are affected by the high incidence of semi-molten/unmelted particles, as demonstrated in Table 2. Porosity is higher at the lower spraying energies, where the semi-molten particles are less deformed. At higher spraying energies, molten material of high diffusivity would fill the asperities and gaps of the previously deposited layers, leading to lower porosities. Hardness increases with spraying power (Fig. 5c), possibly as a result of the porosity decrease [32]. The high increase in the adhesion of the "N" coatings at the highest energy, is attributed to a boost in particle melting, demonstrated by the large decrease in the α-phase content (Table 1).

4. Conclusions

Characterization of air plasma sprayed nanostructured Al_2O_3 ("N"), sintered nanostructured Al_2O_3 ("S") and fused/crushed conventional Al_2O_3 ("C") powders has led to the conclusions:

1. Powder "N" consisted of agglomerates of nanoparticles of average size 93 nm and lattice strain 1.15%.
2. Sintering of the nanopowder at 1100 °C for 2 h, caused surface smoothing, limited coalescence and strain relief.
3. The low melting degree of the nano-feedstock ("N") is attributed to the inherent porosity of the "green" agglomerated nanoparticles.
4. The relatively high melting degree of the "S" coatings is attributed to their tighter microstructure obtained by sintering.
5. The high porosity of the "N" coatings is partly related to the large voids in the interior of the semi-molten particles and partly to their low deformation ability.
6. The "N" coatings presented the lowest adhesion due to the highest porosity and the weakest mechanical anchoring, both direct consequences of the low melting degree.
7. The "S" coatings presented the highest adhesion because they combined a high melting degree with zones of retained nanostructure that can act as crack arresters.
8. Increasing the spray power led to a higher melting degree of the powder and a consequent improvement of the coating properties.

Acknowledgement

D. Zois is grateful for the financial support of the "Hellenic State Scholarships" foundation.

References

[1] H. Gleiter, Nanostruct. Mater. 1 (1992) 1–19.
[2] H. Hahn, Nanostruct. Mater. 2 (1993) 251–265.
[3] R.W. Siegel, Mater. Sci. Forum 235–238 (1997) 851–860.
[4] K. Jia, T.E. Fischer, Wear 203–204 (1997) 310–318.
[5] C.C. Berndt, E.J. Lavernia, J. Therm. Spray Technol. 7 (1998) 411–420.
[6] R.S. Lima, B.R. Marple, Mater. Sci. Eng. A 395 (2005) 269–280.
[7] Y. Zhu, M. Huang, J. Huang, C. Ding, J. Therm. Spray Technol. 8 (1999) 219–222.
[8] J. Karthikeyan, C.C. Berndt, J. Tikkanen, J.Y. Wang, A.H. King, H. Herman, Nanostruct. Mater. 9 (1997) 137–140.
[9] E.H. Jordan, M. Gell, Y.H. Sohn, D. Goberman, L. Shaw, S. Jiang, M. Wang, T.D. Xiao, Y. Wang, P. Strutt, Mater. Sci. Eng. A301 (2001) 80–89.
[10] Y. Wang, S. Jiang, M. Wang, S. Wang, T.D. Xiao, P.R. Strutt, Wear 237 (2000) 176–185.
[11] M. Gell, E.H. Jordan, Y.H. Sohn, D. Goberman, L.L. Shaw, T.D. Xiao, Surf. Coat. Technol. 146–147 (2001) 48–54.
[12] H. Chen, C.X. Ding, Surf. Coat. Technol. 150 (2002) 31–36.
[13] S. Shukla, S. Seal, Nanostruct. Mater. 11 (1999) 1181–1193.
[14] L.L. Shaw, D. Goberman, R. Ren, M. Gell, S. Jiang, Y. Wang, T.D. Xiao, P.R. Strutt, Surf. Coat. Technol. 130 (2000) 1–8.
[15] C. Suryanarayana, Prog. Mater. Sci. 46 (2001) 1–184.
[16] X. Lin, Y. Zeng, S.W. Lee, C. Ding, J. Eur. Ceram. Soc. 24 (2004) 627–634.
[17] A. Agarwal, T. McKechnie, S. Seal, J. Therm. Spray Technol. 12 (2003) 350–359.
[18] L.C. Lim, P.M. Wong, M. Jan, Acta Mater. 48 (2000) 2263–2275.
[19] G.R. Karagedov, N.Z. Lyakhov, Nanostruct. Mater. 11 (1999) 559–572.
[20] A.S.A. Chinelatto, E.M.J.A. Pallone, V. Trombini, R. Tomasi, Ceram. Int. 34 (2007) 2121–2127.
[21] W. Zeng, L. Gao, L. Gui, J. Guo, Ceram. Int. 25 (1999) 723–726.
[22] J.G. Li, X. Sun, Acta Mater. 48 (2000) 3103–3112.
[23] H.P. Klug, L.E. Alexander, X-Ray Diffraction Procedures, 2nd ed., Wiley, New York, 1974.
[24] M.L. Gualtieri, M. Prudenziati, A.F. Gualtieri, Surf. Coat. Technol. 201 (2006) 2984–2989.
[25] H. Schaper, E.B.M. Doesburg, P.H.M. De Korte, L.L. Van Reijen, Solid State Ionics 16 (1985) 261–266.
[26] G.K. Williamson, W.H. Hall, Acta Metall. 1 (1953) 22–31.
[27] B.D. Cullity, Elements of X-Ray Diffraction, Addison-Wesley, 1956.
[28] M. Wang, L.L. Shaw, Surf. Coat. Technol. 202 (2007) 34–44.
[29] J. Zhang, J. He, Y. Dong, X. Li, D. Yan, Rare Metals. 26 (2007) 391–397.
[30] X. Lin, Y. Zeng, X. Zheng, C. Ding, Surf. Coat. Technol. 105 (2005) 85–90.
[31] Z. Karoly, J. Szepvolgyi, Powder Technol. 132 (2003) 211–215.
[32] H. Luo, D. Goberman, L. Shaw, M. Gell, Mater. Sci. Eng. A346 (2003) 237–245.